International Journal of Heat and Mass Transfer 55 (2012) 4638–4650

Contents lists available at SciVerse ScienceDirect

International Journal of Heat and Mass Transfer

journal homepage: www.elsevier.com/locate/ijhmt

An investigation of natural convection of three dimensional horizontal parallel plates from a steady to an unsteady situation by a CUDA computation platform

Wu-Shung Fu *, Wei-Hsiang Wang, Shang-Hao Huang

Department of Mechanical Engineering, National Chiao Tung University, Hsinchu 30010, Taiwan, ROC

ARTICLE INFO

Article history:
Received 13 January 2012
Received in revised form 11 April 2012
Accepted 11 April 2012
Available online 13 May 2012

Keywords:
Natural convection
Horizontal parallel plates
Heat bottom surface
CUDA

ABSTRACT

The heat transfer of natural convection in three dimensional horizontal parallel plates with a heated bottom surface is investigated numerically. For enlarging the application domain, the compressibility of the fluid is taken into consideration instead of the Boussinesq assumption. Numerical methods of the Roe scheme, preconditioning and dual time stepping are adopted for solving governing equations of a low speed compressible flow. A non-reflection condition is used at both apertures in order to decrease computational grids and a CUDA computational platform is developed to economize massive computing time. Variations of thermal and flow fields are examined in detail. The results show that accompanied with elongating the length of the heated bottom surface, both thermal and flow fields are changed from a steady to an unsteady situation.

1. Introduction

Natural convection in opened-ended horizontal parallel plates is a very important subject in both academic and industrial researches such as drying processes, solar receiver systems, fire safety research and the deposition process in semiconductor manufacturing. The location of the heated surface installed on the top or bottom wall of horizontal parallel plates will cause the phenomenon of natural convection to be affected. The installation of the heated surface on the bottom surface is usually more complex than that of the installation on the top surface because of the easy occurrence of unsteadily ascending flow. In this process, the density of the fluid is gradually decreased as the fluid passes over the heat surface. The velocity of the fluid is then steadily accelerated by the variable buoyancy force. As a result, there is a possibility to change the flow field from steady to unsteady in the duration of the heating process that is rather different from the flow field occurring in the forced convection in which an invariable velocity of fluid is assigned by the given condition in advance. Therefore, when this subject is investigated using a numerical study, two thorny problems are observed. One is the treatment of boundary conditions at both opened-ended apertures; The other is the development of a proper and efficient computation method for resolving the variations of the flow and thermal fields from a steady to an unsteady situation during the heating process.

For facilitating theoretical analyses of the subject mentioned above, lots of literature [1–6] adopted the Boussinesq assumption which is available for the temperature differences of natural convection being lower than 30 K [7] to investigate the phenomena of natural convection. According to usage of the Boussinesq assumption, the density of the fluid is regarded as a constant which means the buoyancy force which is a driving force of natural convection is an invariable parameter. The indication of flow field varying from a steady to an unsteady situation caused by the gradual acceleration of flow field in the duration of the heating process mentioned above is difficult to be explained. Those results are useful for a low temperature difference condition but not useful for a high temperature difference condition. Therefore, a previous study [8] abandoned the usage of the Boussinesq assumption and considered the compressibility of the fluid to investigate phenomena of natural convection in a horizontal three dimensional channel. A non-reflecting condition was successfully modified to treat boundary conditions at the opened-ended apertures. Dual reflection phenomena were observed at the opened-ended apertures. Regretfully, the length of the heat wall was too short which resulted in the strength of the buoyancy force not being strong enough, and the variation of flow field from a steady to an unsteady situation being absent. An experimental investigation conducted by Kitamura and Asakawa [9] revealed heat transfer mechanisms of the subject mentioned above. The time-averaged results of local Nusselt numbers were presented and the instantaneously unsteady phenomena were clearly indicated by the thermal field close to the heat wall. The process of variation of flow field from a steady to an unsteady situation was difficult to express because of the limitation of time-averaged experimental results. A similar study was

* Corresponding author. Address: Department of Mechanical Engineering, National Chiao Tung University, 1001 Ta Hsueh Road, Hsinchu 30056, Taiwan, ROC. Tel.: +886 3 5712121x55110; fax: +886 3 5735065.
E-mail address: wsfu@mail.nctu.edu.tw (W.-S. Fu).

0017-9310/$ - see front matter © 2012 Elsevier Ltd. All rights reserved.
http://dx.doi.org/10.1016/j.ijheatmasstransfer.2012.04.022

Nomenclature

A	area (m^2)
d	width of the plate (m)
e	internal energy (J/kg)
g	acceleration of gravity (m/s^2)
h	height of the plate (m)
k	thermal conductivity (W/mK)
k_0	surrounding thermal conductivity (W/mK)
l_1	length of heat surface (m)
l_2	distance between outlet and heat surface (m)
l_3	length of the plate (m)
Nu_x	local Nusselt number defined in Eq. (28) $Nu_x = \frac{h}{k_0(T_h - T_c)}\left[k(T)\frac{\partial T}{\partial y}\right]$
$\overline{Nu}_x$	time average local Nusselt number defined in Eq. (29) $\overline{Nu}_x = \frac{1}{t}\int_t Nu_x dt$
$\overline{Nu}_A$	area average local Nusselt number defined in Eq. (30) $\overline{Nu}_A = \frac{1}{A}\int_d \int_{l_1} Nu_x dx dz$
$\overline{Nu}$	average Nusselt number defined in Eq. (31) $\overline{Nu} = \frac{1}{A}\int_d \int_{l_1} \overline{Nu}_x dx dz$
P	pressure (Pa)
P_0	surrounding pressure (Pa)
Pr	Prandtl number
R	gas constant (J/kg/K)
R^*	length ratio $R^* = \frac{l_1}{h}$
Ra	Rayleigh number defined in Eq. (26) $Ra = \Pr\frac{g\rho_0^2(T_h - T_c)h^3}{T_0\mu(T)^2}$
Ra^*	modified Rayleigh number defined in Eq. (27) $Ra^* = Ra \times \frac{l_1}{h}$
Re	Reynolds number
t	time (s)
t^*	dimensionless time $t^* = t\frac{\mu_0}{\rho_0 h^2}$
T	temperature (K)
T_0	temperature of surroundings (K)
T_h	temperature of heat surface (K)
u, v, w	velocities in x, y and z directions (m/s)
U, V, W	dimensionless velocities $U = \frac{u}{\sqrt{Ra^*}\frac{\alpha}{h}}$, $V = \frac{v}{\sqrt{Ra^*}\frac{\alpha}{h}}$, $W = \frac{w}{\sqrt{Ra^*}\frac{\alpha}{h}}$
x, y, z	Cartesian coordinates (m)
X, Y, Z	dimensionless Cartesian coordinates $X = \frac{x}{l_3}$, $Y = \frac{y}{l_3}$ and $Z = \frac{z}{l_3}$

Greek symbols

α	thermal diffusivity rate (m^2/s)
ρ	density (kg/m^3)
ρ_0	surrounding density (kg/m^3)
μ	viscosity ($N\,s/m^2$)
μ_0	surrounding viscosity ($N\,s/m^2$)
γ	specific heat ratio

conducted by Turgut and Onur [10]. A code was used to execute numerical calculation to validate the experimental results auxiliarily. The results revealed that the increment of the average Nusselt number accompanied with the increment of the separation distance. Both results of numerical and experimental works had good agreements. Due to the presentation of time- averaged results, the phenomenon of unsteady natural convection was not discussed. Yang et al. [11] investigated the thermal fluid instability between two horizontal parallel plates with three different thermal condition cases numerically. The phenomenon of instability was mainly induced by a thermal perturbation of temperature obtained from a Goussian random number generator. The results showed that the total fluid kinetic energy in the domain converged for the top heating case, but diverged for the other two cases. Because of the preliminary assignment of perturbation condition, the process of stability changing to instability could not be indicated. Manca et al. [12] and Manca and Nardini [13] conducted experimental works to investigate natural convection in horizontal channels and parallel plates, respectively. Their main results indicated phenomena of flow fields and temperature profiles under different thermal conditions. A flow pattern of a C shape presented in each mode. Instantaneously detailed results, including steady and unsteady situations, were separately indicated. Due to the limitations of time-averaged results mentioned above, the realistic and important phenomena of natural convection varying from a steady to an unsteady situation in a heating process are hardly studied.

The aim of the study, which involves the changing of the length of the heated surface investigates variation processes of natural convection of three dimensional horizontal parallel plates from a steady to an unsteady situation numerically. In order to simulate the subject more realistically, the Boussinesq assumption is not adopted, and instead, the compressibility of the fluid is taken into consideration. The buoyancy force is then to vary with the heating process and exerts a force on the fluid to change its buoyancy force from a weak to a strong state gradually affecting the variation of flow and thermal fields from a steady to an unsteady. The time needed for computation and date acquisition is extremely huge, and an effective method of a CUDA computation platform [14] is then used for executing parallel computation. Solution methods of the Roe [15], preconditioning [16] and dual time stepping [17] for solving a low speed compressible fluid flow in a transient state are combined together. As well, a modified method [8] is used to treat the reflection problems occurring at apertures of parallel plates. The results reveal that accompanied with the increment of increase of the heated surface length, the flow field varies from a steady to an unsteady situation. Phenomena of an unsteady situation easily occur along the longer heat surface and are similar to a

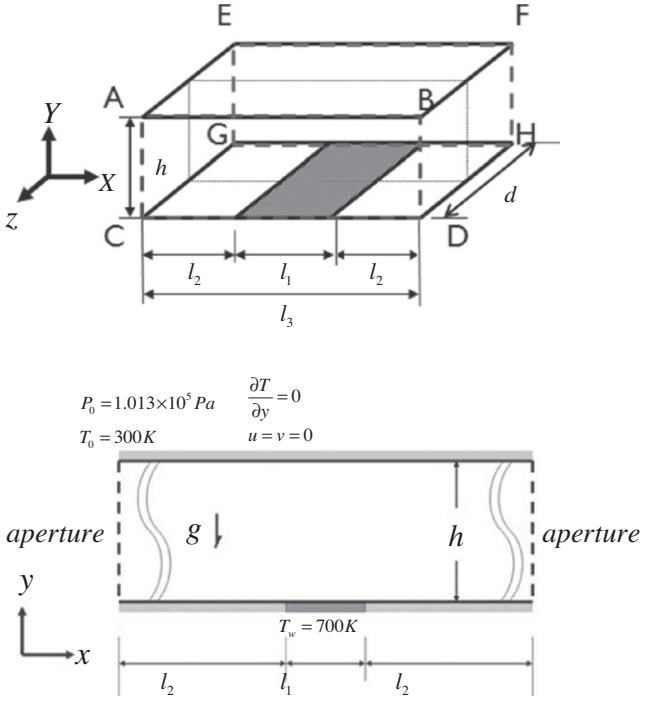

Fig. 1. Physical model.

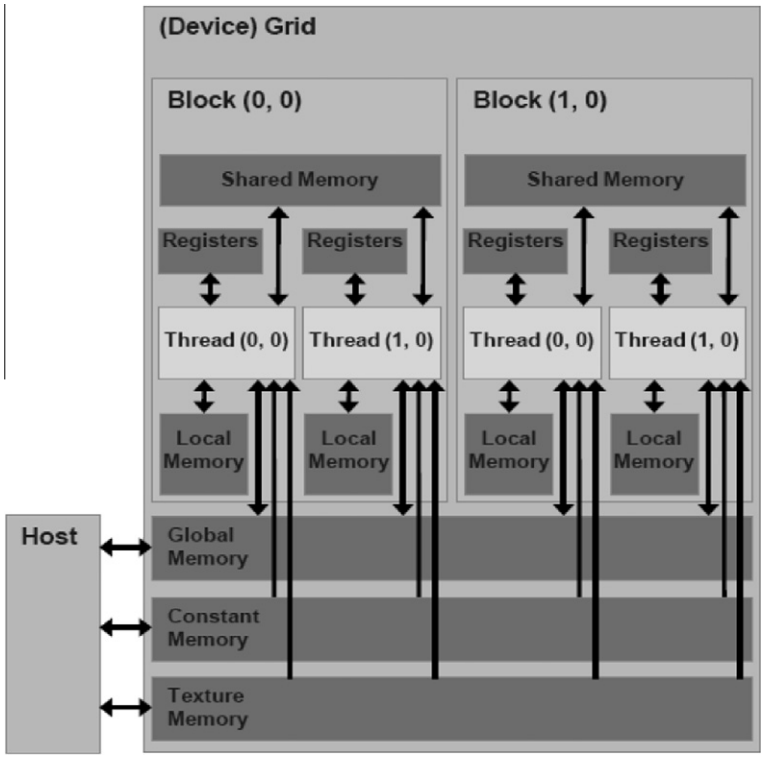

Fig. 2. Schematic diagram of CUDA platform [14].

periodic motion which naturally causes the variation of the local Nusselt numbers to be periodic.

2. Physical model

A physical model of three dimensional parallel plates is indicated in Fig. 1. The total length and height of the physical model are l_3 and h, respectively. On the bottom plate, lengths of l_1 and l_2 are the heated and adiabatic walls, respectively.

The temperature of the heated wall is T_h, and the top plate is adiabatic. The width of the physical model is d, and the direction of gravity is downward. Boundary conditions on both apertures are non-reflecting conditions and both sides of the width are periodic conditions. The pressure and temperature of the outside of parallel plates are 101300 Pa and 298 K, respectively.

For facilitating the analysis, the following assumptions are made.

1. The work fluid is ideal gas and follows the equation of state of ideal gas.
2. Magnitudes of gradients of density and pressure on the whole surfaces in the normal direction are zero.

The governing equations are expressed as follows.

$$\frac{\partial U}{\partial t}+\frac{\partial F}{\partial x}+\frac{\partial G}{\partial y}+\frac{\partial H}{\partial z}=S \tag{1}$$

Table 1
Comparison of computing efficiency.

Type	CPU Intel Quad Q6600 (4 core)	CPU Intel Core i5 (4 core)	GPU Nvidia Tesla C1060
Grids	$220\times160\times10$	$220\times160\times10$	$220\times160\times10$
Parallel method	OpenMp	OpenMp	CUDA
s/step	76.14	26.3	10.88
Scaling	1	2.7	7

and the state equation of ideal gas is used.

$$P=\rho RT \tag{2}$$

The terms included in U, F, G, H and S are separately shown in the following equations.

$$U=\begin{bmatrix}\rho\\ \rho u\\ \rho v\\ \rho w\\ \rho E\end{bmatrix} \tag{3}$$

$$\left.\begin{aligned}
F&=\begin{bmatrix}\rho u\\ \rho u^2+P-\tau_{xx}\\ \rho uv-\tau_{xy}\\ \rho uw-\tau_{xz}\\ \rho Eu+Pu-k\frac{\partial T}{\partial x}-u\tau_{xx}-v\tau_{xy}-w\tau_{xz}\end{bmatrix}\\
G&=\begin{bmatrix}\rho v\\ \rho uv-\tau_{yx}\\ \rho v^2+P-\tau_{yy}\\ \rho vw-\tau_{yz}\\ \rho Ev+Pv-k\frac{\partial T}{\partial y}-u\tau_{yx}-v\tau_{yy}-w\tau_{yz}\end{bmatrix}\\
H&=\begin{bmatrix}\rho w\\ \rho uw-\tau_{zx}\\ \rho vw-\tau_{zy}\\ \rho w^2+P-\tau_{zz}\\ \rho Ew+Pw-k\frac{\partial T}{\partial z}-u\tau_{zx}-v\tau_{zy}-w\tau_{zz}\end{bmatrix}\\
S&=\begin{bmatrix}0\\ 0\\ -(\rho-\rho_0)g\\ 0\\ -(\rho-\rho_0)gv\end{bmatrix}
\end{aligned}\right\} \tag{4}$$

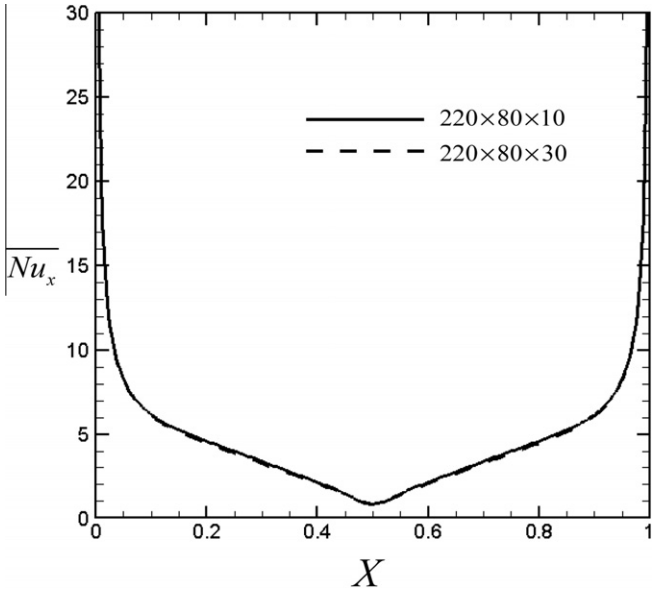

Fig. 3. Selection of grid distribution in Z direction ($R^* = \frac{11}{4}$).

Sutherland's law is adopted to evaluate the viscosity and thermal conductivity shown as follows.

$$\mu(T) = \mu_0 \left(\frac{T}{T_0}\right)^{\frac{2}{3}} \frac{T_0 + 110}{T + 110} \tag{5}$$

$$k(T) = \frac{\mu(T)\gamma R}{(\gamma - 1)\mathrm{Pr}} \tag{6}$$

in which

$$E = \frac{P}{\rho(\gamma - 1)} + \frac{1}{2}(u^2 + v^2 + w^2) \tag{7}$$

$\rho_0 = 1.1842\ \mathrm{kg/m^3}$, $g = 9.81\ \mathrm{m/s^2}$

$\mu_0 = 1.85 \times 10^{-5}\ \mathrm{N\,s/m^2}$, $T_0 = 298.05\ \mathrm{K}$

$\gamma = 1.4$, $R = 287\ \mathrm{J/kg/K}$, $\mathrm{Pr} = 0.72$

3. Numerical method

The Roe scheme and preconditioning method are used to solve the governing equations of a compressible flow shown in Eq. (1). Also, the method of dual time stepping is added to calculate the transient state. And Eq. (1) can be obtained.

$$\Gamma \frac{\partial U_p}{\partial \tau} + \frac{\partial U}{\partial t} + \frac{\partial F}{\partial x} + \frac{\partial G}{\partial y} + \frac{\partial H}{\partial z} = S \tag{8}$$

where τ is the artificial time, t is the physical time. Γ is a preconditioning matrix proposed by Weiss and Smith[16] and U_p is a primitive form of $[\rho, \rho u, \rho v, \rho w, \rho e]^T$.

Discretization of Eq. (8) is executed. The terms of $\frac{\partial U_p}{\partial \tau}$ and $\frac{\partial U}{\partial t}$ are differentiated by a first-order forward difference and a second-order backward difference, respectively, and the terms of $\frac{\partial F}{\partial x}$, $\frac{\partial G}{\partial y}$, and $\frac{\partial H}{\partial z}$ are differentiated by a central difference, the following equation can be obtained.

$$\Gamma \frac{U_p^{k+1} - U_p^k}{\Delta \tau} + \frac{3U^{n+1} - 4U^n + U^{n-1}}{2\Delta t} + \frac{1}{\Delta x}\left(F^{k+1}_{i+\frac{1}{2},j,k} - F^{k+1}_{i-\frac{1}{2},j,k}\right) + \frac{1}{\Delta y}\left(G^{k+1}_{i,j+\frac{1}{2},k} - G^{k+1}_{i,j-\frac{1}{2},k}\right) + \frac{1}{\Delta z}\left(H^{k+1}_{i,j,k+\frac{1}{2}} - H^{k+1}_{i,j,k-\frac{1}{2}}\right) = S \tag{9}$$

The terms of U^{k+1} and F^{k+1} in Eq. (9) are necessary to be linearized and expressed as follows.

$$U^{k+1} = U^k + M\Delta U_p \tag{10}$$

in which $M = \frac{\partial U}{\partial U_p}$ and $A_p = \frac{\partial F^k}{\partial U_p}$

$$F^{k+1} = F^k + A_p \Delta U_p \tag{11}$$

where $A_p = \frac{\partial F}{\partial U_p}$ is the flux jacobian and the same methods for $B_p = \frac{\partial G}{\partial U_p}$ and $C_p = \frac{\partial H}{\partial U_p}$ are used in linearization of G^{k+1} and H^{k+1}, respectively.

To substitute Eqs. (10) and (11) into Eq. (9), the following equation is derived.

$$\left[\frac{I}{\Delta \tau} + \Gamma^{-1} M \frac{3}{2\Delta t} + \Gamma^{-1}\left(\delta_x A_p^k + \delta_y B_p^k + \delta_z C_p^k\right)\right]\Delta U_p = \Gamma^{-1} R^k \tag{12}$$

where δ_x, δ_y, and δ_z are central-difference operators and

$$R^k = S - \left(\frac{3U^k - 4U^n + U^{n-1}}{2\Delta t}\right) - (\delta_x F^k + \delta_y G^k + \delta_z H^k)$$

The solver of Eq. (13) is the LUSGS implicit method proposed by Yoon and Jamesont [18].

$$\begin{aligned} A_p &= \Gamma^{-1} A_p^k \\ B_p &= \Gamma^{-1} B_p^k \\ C_p &= \Gamma^{-1} C_p^k \end{aligned} \tag{13}$$

Eq. (12) can be rearranged as follows.

$$(L + D + U)\Delta U_p = \Gamma^{-1} R^k \tag{14}$$

where

$$\left.\begin{aligned} L &= -\left[\tfrac{1}{\Delta x}\left(A_p^+\right)_{i-1,j,k} + \tfrac{1}{\Delta y}\left(B_p^+\right)_{i,j-1,k} + \tfrac{1}{\Delta z}\left(C_p^+\right)_{i,j,k-1}\right] \\ D &= \tfrac{I}{\Delta \tau} + \Gamma^{-1} M \tfrac{3}{2\Delta t} + \left\{\tfrac{1}{\Delta x}\left[\left(A_p^+\right)_{i,j,k} - \left(A_p^-\right)_{i,j,k}\right] + \tfrac{1}{\Delta y}\left[\left(B_p^+\right)_{i,j,k} - \left(B_p^-\right)_{i,j,k}\right] + \tfrac{1}{\Delta z}\left[\left(C_p^+\right)_{i,j,k} - \left(C_p^-\right)_{i,j,k}\right]\right\} \\ U &= \left[\tfrac{1}{\Delta x}\left(A_p^-\right)_{i+1,j,k} + \tfrac{1}{\Delta y}\left(B_p^-\right)_{i,j+1,k} + \tfrac{1}{\Delta z}\left(C_p^-\right)_{i,j,k+1}\right] \end{aligned}\right\} \tag{15}$$

As for the computation of $R^k = S - \left(\frac{3U^k - 4U^n + U^{n-1}}{2\Delta t}\right) - (\delta_x F^k + \delta_y G^k + \delta_z H^k)$ in the right hand side (RHS) of Eq. (12), the terms in-

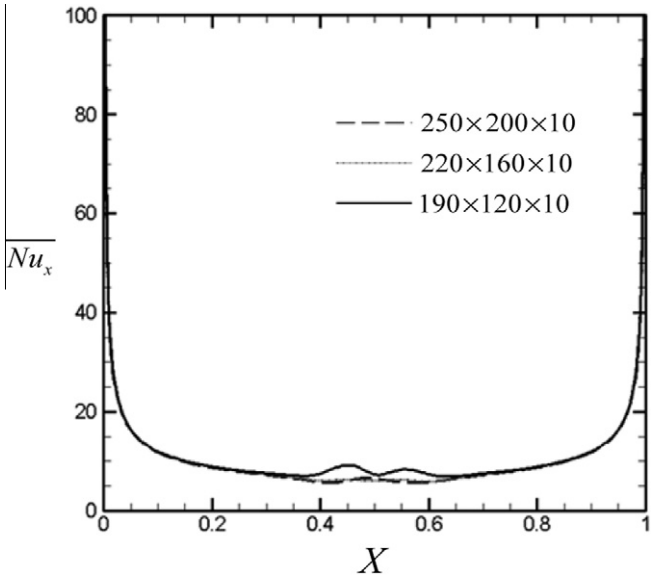

Fig. 4. Comparison of different grid distributions.

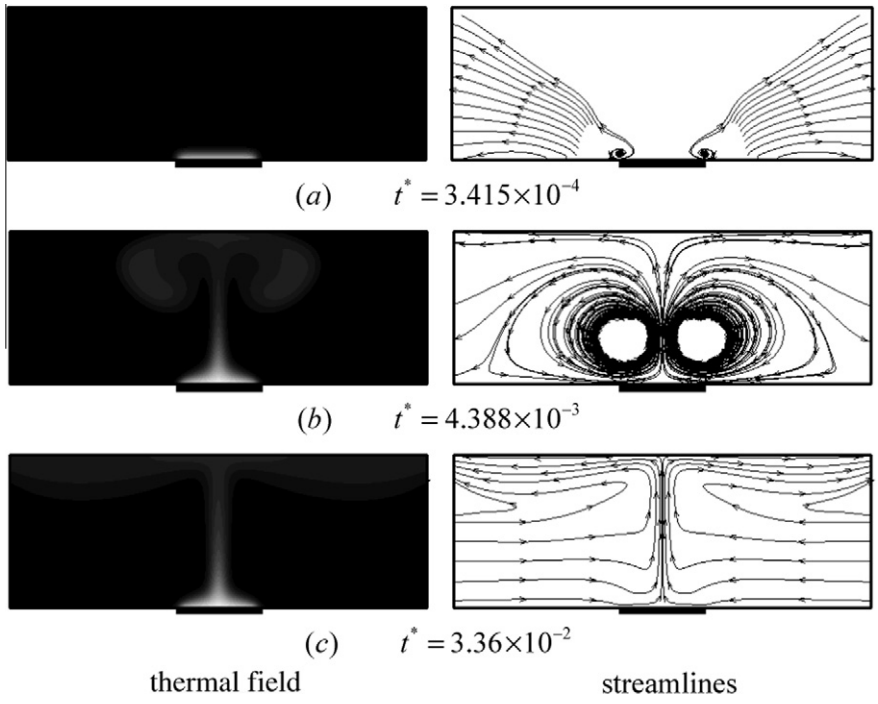

Fig. 5. Histories of development of thermal field and streamlines under $Ra^* = 1.58 \times 10^6$.

cluded in F shown in Eq. (4) based on Cartesian coordinates can be divided into two parts. One is the inviscid term $F_{inviscid}$ and the other is the viscous term $F_{viscous}$.

$$F = F_{inviscid} + F_{viscous} = \begin{Bmatrix} \rho u \\ \rho u^2 + p \\ \rho u v \\ \rho u w \\ \rho\left(e + \frac{V^2}{2}\right)u + pu - k\frac{\partial T}{\partial x} \end{Bmatrix} - \begin{Bmatrix} 0 \\ \tau_{xx} \\ \tau_{xy} \\ \tau_{xz} \\ +u\tau_{xx} + v\tau_{xy} + w\tau_{xz} \end{Bmatrix} \tag{16}$$

The upwind difference scheme developed by Roe [15] is employed in discretization of the term of $F_{inviscid}$ at the interface cells $(i+\frac{1}{2})$ and expressed as follows at a low Mach number situation.

$$F_{inviscid,i+\frac{1}{2}} = \frac{1}{2}(F_R + F_L) - \frac{1}{2}|\Gamma^{-1}AM|\Delta U_P \tag{17}$$

The third-order MUSCL scheme proposed by Abalakin et al. [19] is used to compute the term of $F_{inviscid}$. And a fourth central difference is adopted to calculate the magnitudes of the viscous terms and the related derivations are indicated as follows.

$$\frac{\partial u}{\partial x} = \frac{u_{i-2} - 8u_{i-1} + 8u_{i+1} - u_{i+2}}{12\Delta x} + o(\Delta x^4) \tag{18}$$

And the same methods for G and H are used, respectively.

On the adiabatic surface, the boundary conditions are

$$\begin{aligned} P(i,0,k) &= P(i,1,k) \\ u(i,0,k) &= -u(i,1,k) \\ v(i,0,k) &= -v(i,1,k) \\ w(i,0,k) &= -w(i,1,k) \\ T(i,0,k) &= T(i,1,k) \end{aligned} \tag{19}$$

$$\begin{aligned} P(i,ny+1,k) &= P(i,ny,k) \\ u(i,ny+1,k) &= u(i,ny,k) \\ v(i,ny+1,k) &= v(i,ny,k) \\ w(i,ny+1,k) &= w(i,ny,k) \\ T(i,ny+1,k) &= T(i,ny,k) \end{aligned} \tag{20}$$

On the heated surface, the boundary conditions are

$$\begin{aligned} P(i,0,k) &= P(i,1,k) \\ u(i,0,k) &= -u(i,1,k) \\ v(i,0,k) &= -v(i,1,k) \\ w(i,0,k) &= -w(i,1,k) \\ T(i,0,k) &= 2T_h - T(i,1,k) \end{aligned} \tag{21}$$

where T_h is the wall temperature.

0 indicates the ghost cell and 1 indicates the cell closest to the wall.

As for the boundary conditions at the apertures of the channel, in order to avoid a low speed of compressible flow in the channel to be polluted by the reflections of acoustic waves, the non-reflecting boundary conditions are then necessarily used at the apertures of the channel.

In a high speed compressible flow condition, the method of LODI (local one dimensional inviscid relations) proposed by Poinsot and Lele [20] was suitably adopted for determining the nonreflecting boundary conditions at the apertures of the channel. However, a preconditioning matrix is not used in the above method that causes the method to be not available for determining the non-reflecting boundary conditions at the apertures of the channel under a low speed compressible flow. As a result, the modification of the above method [8] is adopted for resolving the non-reflection boundary conditions under an extremely low speed compressible flow.

Along the Z direction, periodic conditions are used, and then the boundary conditions of surfaces of ABCD and EFGH shown in Fig. 1 can be expressed as the following equations, respectively.

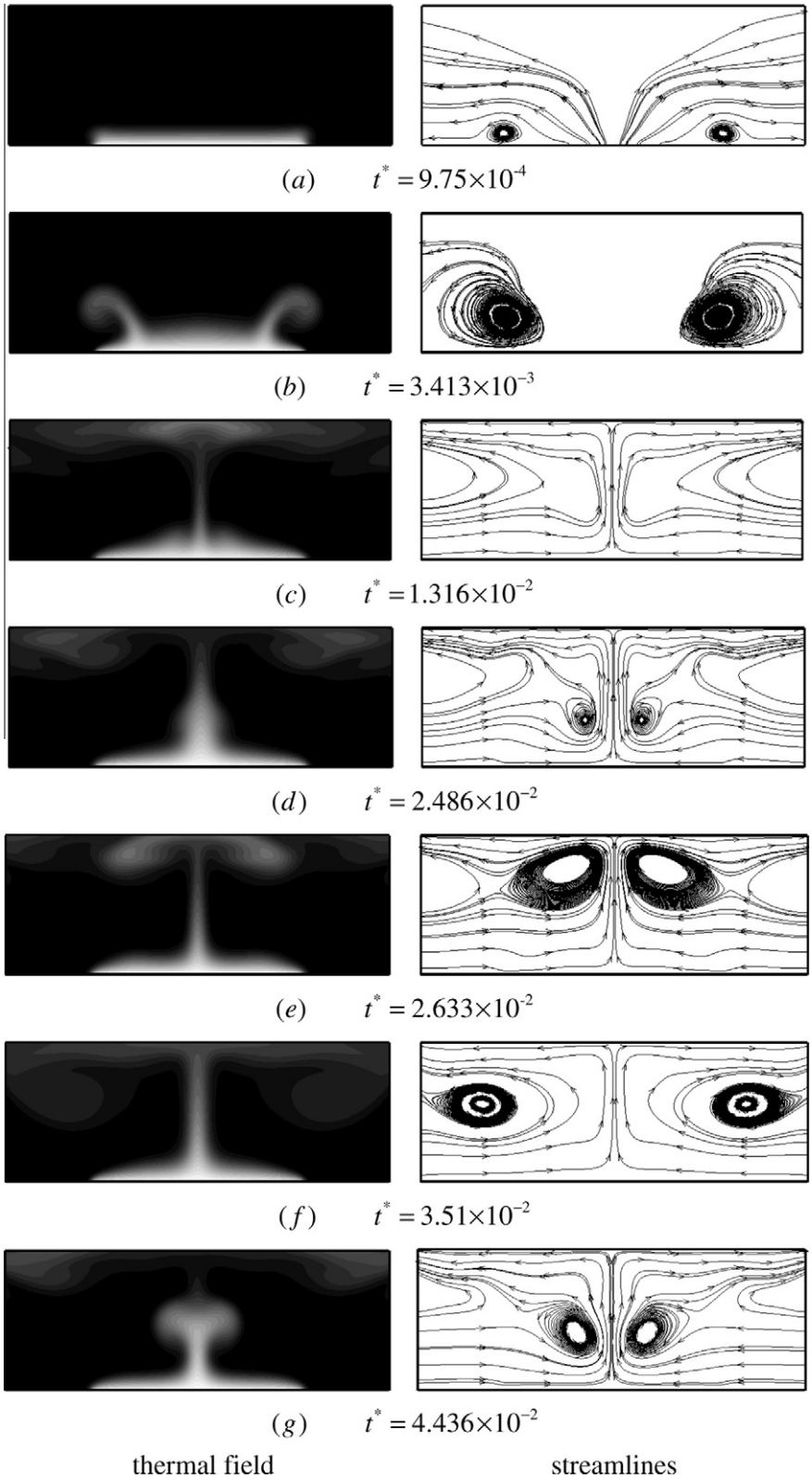

Fig. 6. Histories of development of thermal field and streamlines under $Ra^* = 4.73 \times 10^6$.

$$\begin{aligned} P(i,j,0) &= P(i,j,nz) \\ u(i,j,0) &= u(i,j,nz) \\ v(i,j,0) &= v(i,j,nz) \\ w(i,j,0) &= w(i,j,nz) \\ T(i,j,0) &= T(i,j,nz) \end{aligned} \tag{22}$$

$$\begin{aligned} P(i,j,nz+1) &= P(i,j,1) \\ u(i,j,nz+1) &= u(i,j,1) \\ v(i,j,nz+1) &= v(i,j,1) \\ w(i,j,nz+1) &= w(i,j,1) \\ T(i,j,nz+1) &= T(i,j,1) \end{aligned} \tag{23}$$

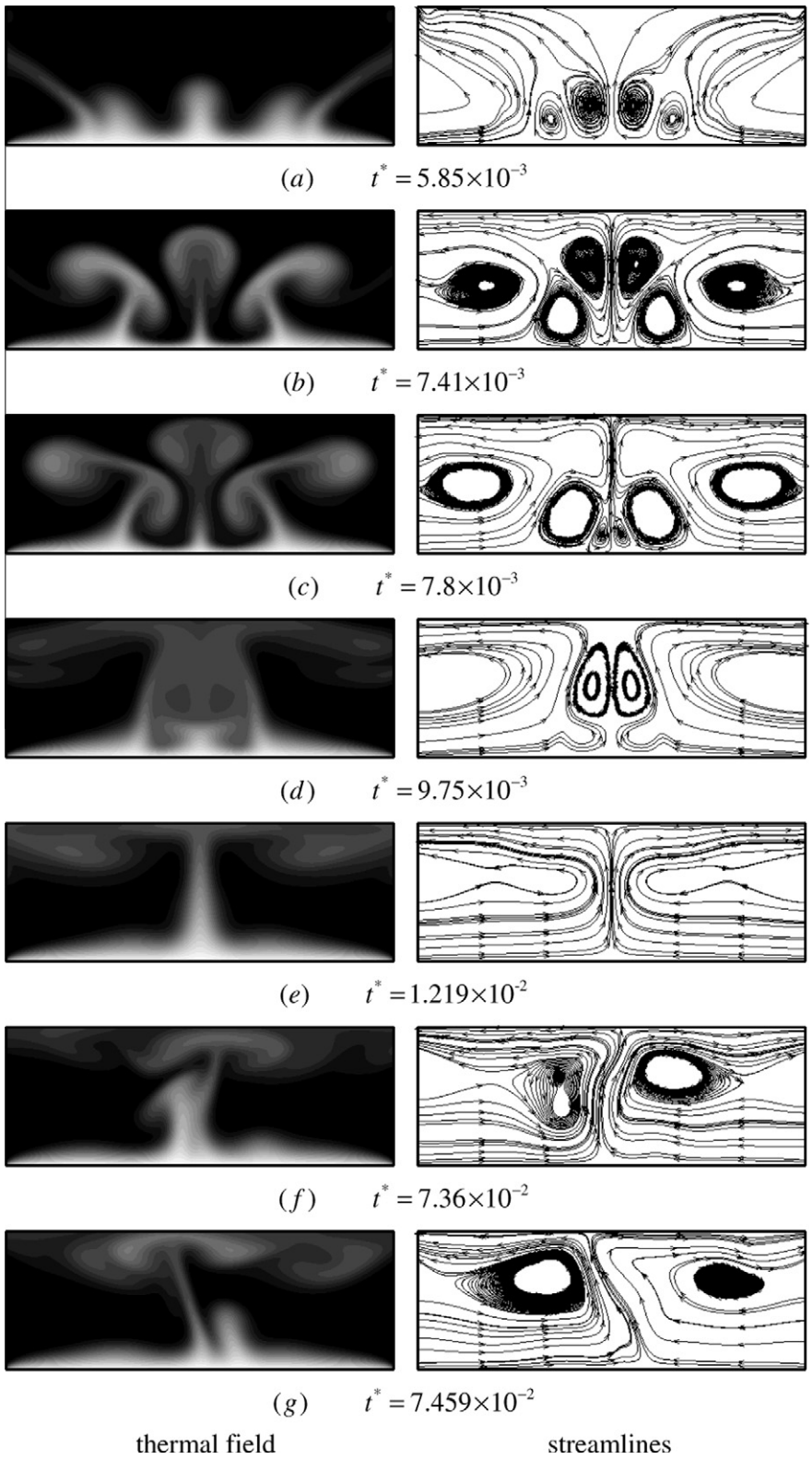

Fig. 7. Histories of development of thermal field and streamlines under $Ra^* = 8.66 \times 10^6$.

0 indicates the cell at the ABCD surface and nz + 1 indicates the cell at the EFGH surface.

A procedure calculating the equations mentioned above is briefly described as follows.

(1) Assign the initial conditions of pressure, velocities and temperatures.
(2) Use the MUSCL method to calculate Eq. (12) to obtain the magnitude of ΔU_p.
(3) Substitute the magnitude of ΔU_p into Eq. (17) and use the Roe method to calculate the magnitudes of inviscid terms of $F_{inviscid}$.
(4) Calculate Eq. (18) to obtain the magnitudes of viscous terms and substitute in Eq. (16).

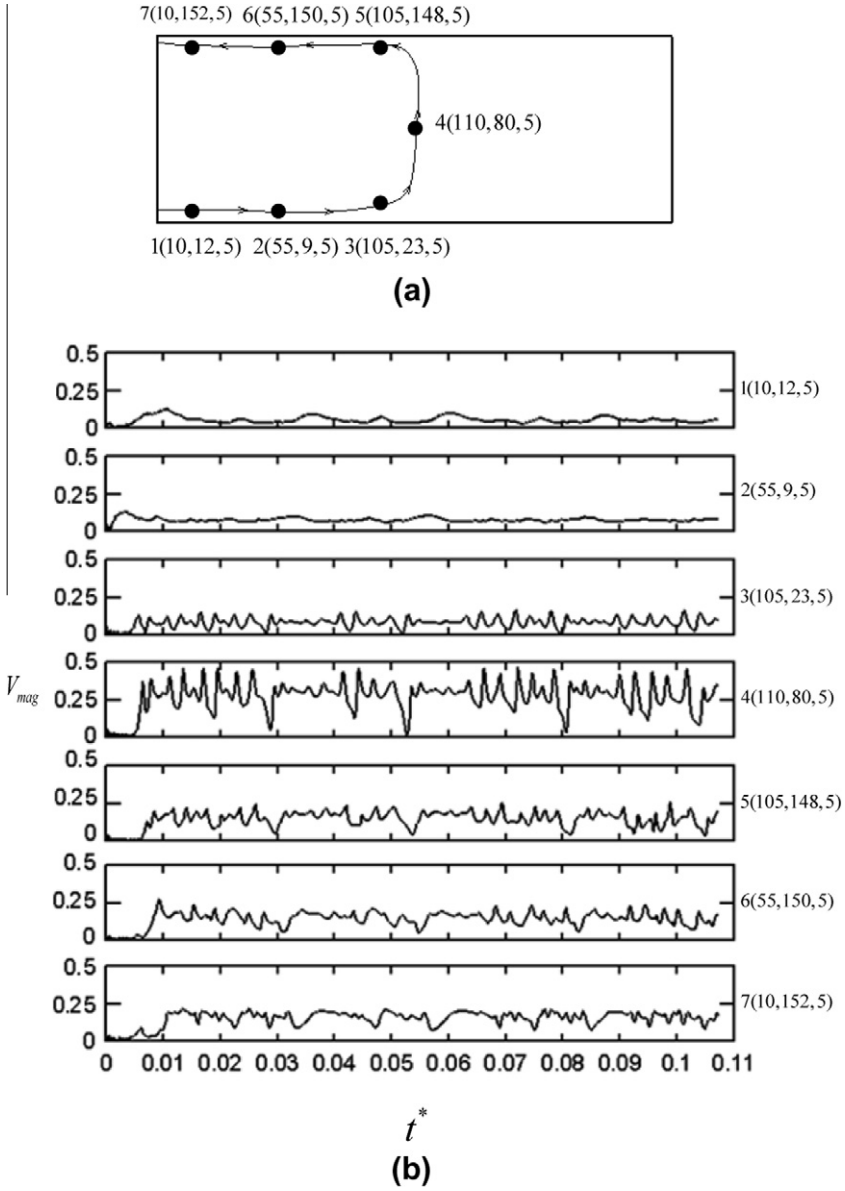

Fig. 8. Variations of local resultant velocity V_{mag} at different locations of a time average streamline under $Ra^* = 4.73 \times 10^6$.

(5) Solve U_p^{k+1}.

$$U_p^{k+1} = U_p^k + \Delta U_p^k \tag{24}$$

(6) Calculate Eq. (9) and examine the convergence of the iterational computation of U_p^{k+1}. Repeat (2)–(5) until $\frac{U_p^{k+1} - U_p^k}{\Delta\tau} < \varepsilon$, $\varepsilon = 10^{-3}$.

The time of computation and date acquisition is extremely huge, and an effective method of a CUDA computation platform is then used for executing parallel computation. The main function of the CUDA computation platform [14], which is a kind of integrated technique developed by NVIDIA company, is to integrate the performance of a GPU (graphics processing unit) arrayed in a video card installed in a host computer to a numerical parallel computation processor executed in the host computer.

A brief description of usage of the CUDA is indicated as follows. Three steps have been executed and Fig. 2 is the schematic diagram. The first step is that the data are moved from the memory of the host to the memory in the graphic hardware. Then the GPU is utilized to compute. The general method of assigning numbers in three dimensional grids is a three dimensional matrix (i,j,k). However, it will be very complicated to move the data from the host to the graphic hardware if the three dimensional matrix is adopted. Therefore, it is necessary to transport the three dimensional matrix to the one dimensional matrix. Then, the data will be easy to be moved. The equation of transporting is showed in the following process.

$$\text{Device (assign numbers)} = \text{host } (i \times ny \times nz + j \times nz + k) \tag{25}$$

where nx, ny and nz are the numbers of grids in the x, y and z direction, respectively.

The second step is to parallel the program. The best advantage of the graphic hardware is that there are multiple cores in it to execute the computation. Then the program paralleling is absolutely necessary.

The third step is to move the results computed by GPUs from the graphic hardware to the host and transform the one dimensional matrix to the original three dimensional matrix. Performance tests of CUDA computation platforms are tabulated in

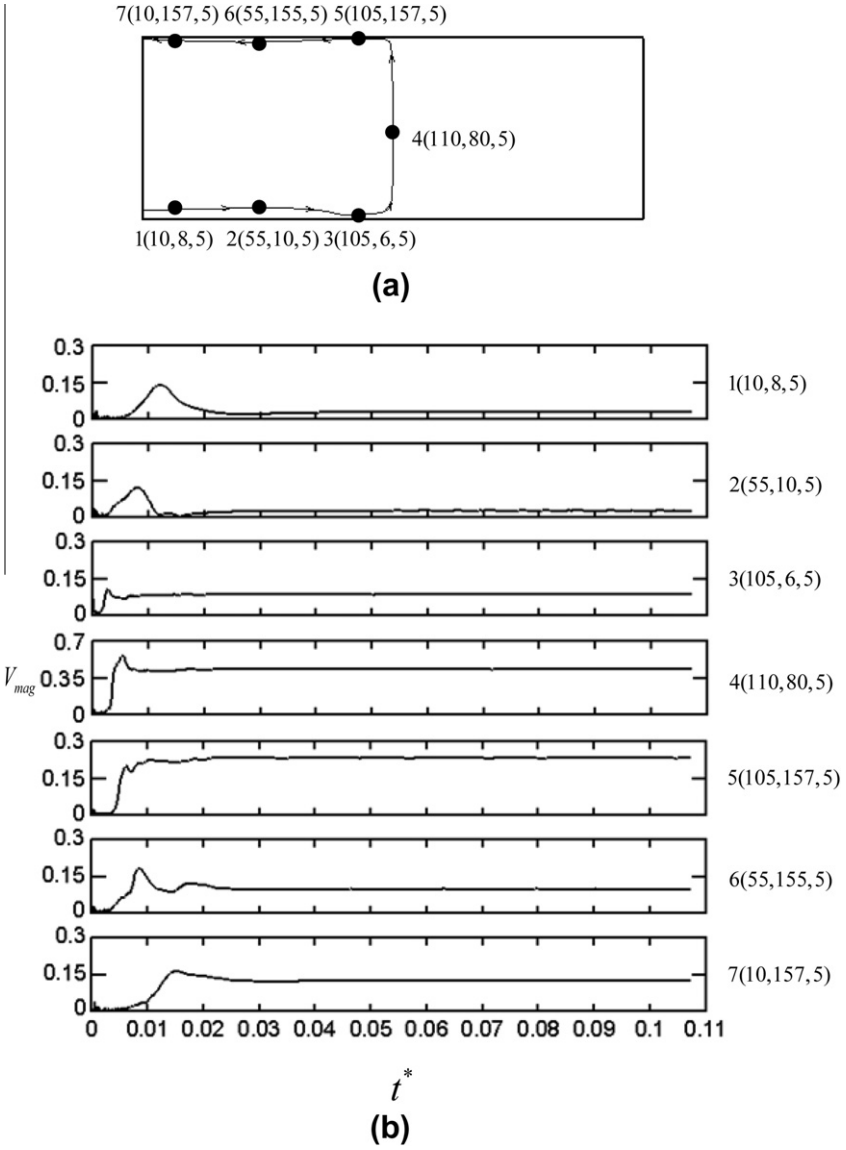

Fig. 9. Variations of local resultant velocity V_{mag} at different locations of a time average streamline under $Ra^* = 1.58 \times 10^6$.

Table 1, and the results are remarkable. The computational time consumed by the most complicated case is about three weeks.

4. Results and discussion

The height of parallel plates is usually regarded as a characteristic length when the Rayleigh number is used in a parallel plates problem and defined as follows.

$$Ra = \mathrm{Pr}\frac{g\rho_0^2(T_h - T_c)h^3}{T_0\mu(T)^2} \tag{26}$$

However, the length of heated bottom wall affects heat transfer phenomena remarkably. In order to highlight the influence of the length of the heat wall, a modified Rayleigh number Ra^* is newly defined in the following equation.

$$Ra^* = Ra \times \frac{L_1}{h} \tag{27}$$

In this study, three different magnitudes of $R^* = \frac{L_1}{h}$ are considered, and they are $\frac{1}{2}(Ra^* = 1.58 \times 10^6)$, $\frac{3}{2}(Ra^* = 4.73 \times 10^6)$ and $\frac{11}{4}(Ra^* = 8.66 \times 10^6)$.

In Fig. 3, in order to ensure the accuracy of the observations of the three dimensional phenomena and because of the limitations of the amounts of computational grids, time-averaged local Nusselt numbers $\overline{Nu}_x's$ distributed on the heated bottom surface of the central cross section of the xy plane are indicated by two different computational grids of $220 \times 80 \times 30$ and $220 \times 80 \times 10$. The definitions of local and time-averaged local Nusselt numbers of Nu_x and $\overline{Nu}_x$ are expressed as follows, respectively.

$$Nu_x = \frac{h}{k_0(T_h - T_c)}\left[k(T)\frac{\partial T}{\partial y}\right] \tag{28}$$

$$\overline{Nu}_x = \frac{1}{t}\int_t Nu_x dt \tag{29}$$

According to the results, 10 grids arrayed in the Z direction are selected. The results of grid tests of appropriate grids arrayed in X and Y directions are shown in Fig. 4. The distribution of grids of $220 \times 160 \times 10$ is determined and used to obtain the following results.

Shown in Fig. 5, histories of development of thermal fields and streamlines are indicated under the $Ra^* = 1.58 \times 10^6$ situation. The

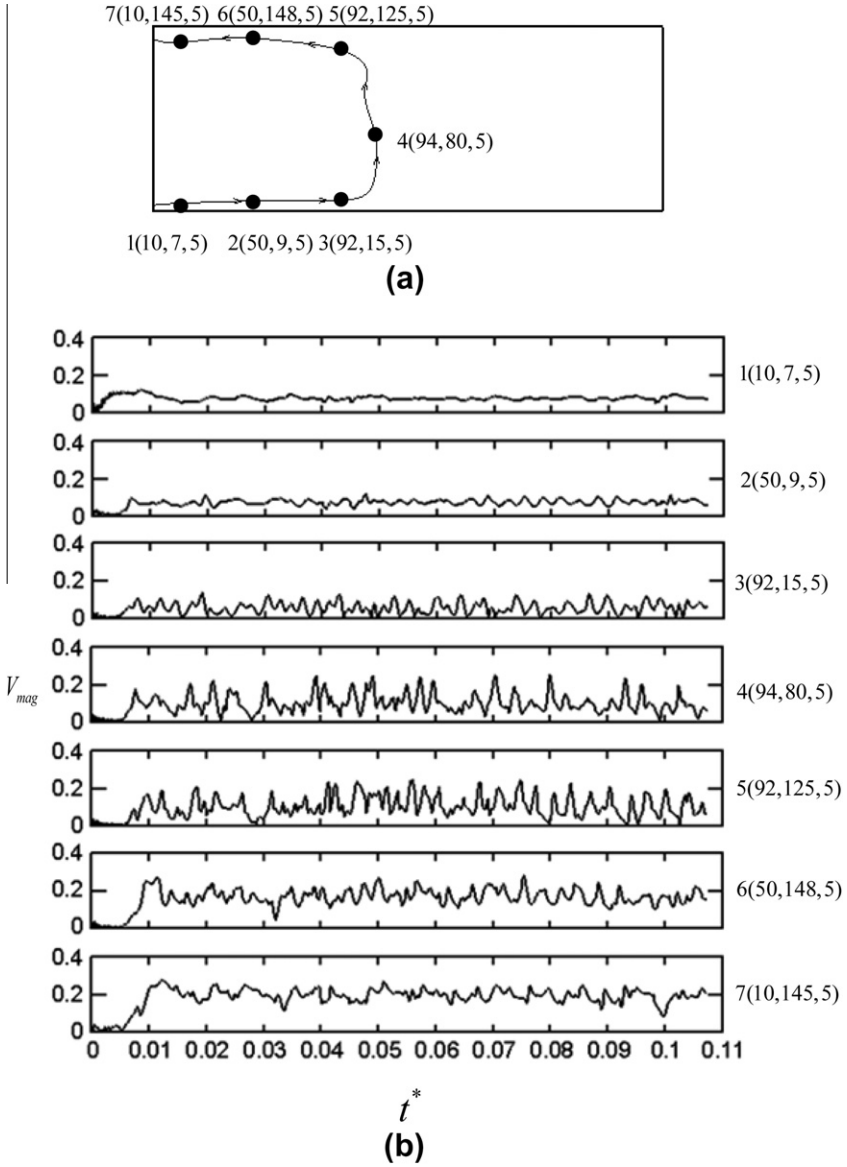

Fig. 10. Variations of local resultant velocity V_{mag} at different locations of a time average streamline under $Ra^* = 8.66 \times 10^6$.

darker the color is, the lower the temperature displays. The temperature of the heated surface is instantaneously raised to 700 K when the computation process is executed. At the initial stage ($t^* = 3.415 \times 10^{-4}$), the heat conduction mode dominates the heat transfer mechanism. Fluids close to the heat wall are heated and expanded, and then part of the fluids are discharged through the apertures. In the next stage ($t^* = 4.388 \times 10^{-3}$), heated fluids with light density exerted by the buoyancy force ascend to the top wall. Ascending fluids impinge the top wall and separately flow to both apertures. Meanwhile part of the ascending fluids form two symmetrical circulations. Afterward ($t^* = 3.36 \times 10^{-2}$), thermal and flow fields incline to a steady situation. Phenomena of both fields indicate a typical natural convection mode.

In Fig. 6, histories of development of thermal fields and streamlines are shown under the $Ra^* = 4.73 \times 10^6$ situation. The larger magnitude of Ra^* corresponds with an increase in the length of the heated wall which naturally causes natural convection phenomena to be more active. In the three initial stages of (a)–(c), the variations of thermal fields and streamlines of this situation are similar to those shown in the former situation of Fig. 5. Afterward, shown in Fig. 6(d) ascending fluids along the longer heated bottom wall continuously accumulate and start to form two small circulations. Right after the two small circulations which gradually attract some fluids on the way to the top wall, they increase in size shown in Fig. 6(e). In Fig. 6(f), two big circulations are expelled by the other ascending fluids and flow to both apertures. Not long after, in Fig. 6(g) two small circulations similar to those shown in Fig. 6(d) periodically appear in the region near the heated bottom wall, and the similar development from Fig. 6(d) to (f) uninterruptedly displays. These behaviors are similar to periodic motion and rather different from those shown in Fig. 5. In this situation, the symmetrical developments of thermal and flow fields based on the center line are characteristic.

As the magnitude of the Ra^* is equal to 8.66×10^6, the whole bottom surface is heated. The corresponding histories of development of thermal and flow fields are shown in Fig. 7. The variations of thermal and flow fields of the initial stages ahead of the time of $t^* = 5.85 \times 10^{-3}$ are somewhat similar to those shown in the corresponding initial stages of Figs. 5 and 6. In Fig. 7(a), t^* is equal to 5.85×10^{-3}. Since the heated bottom surface is long, two couples

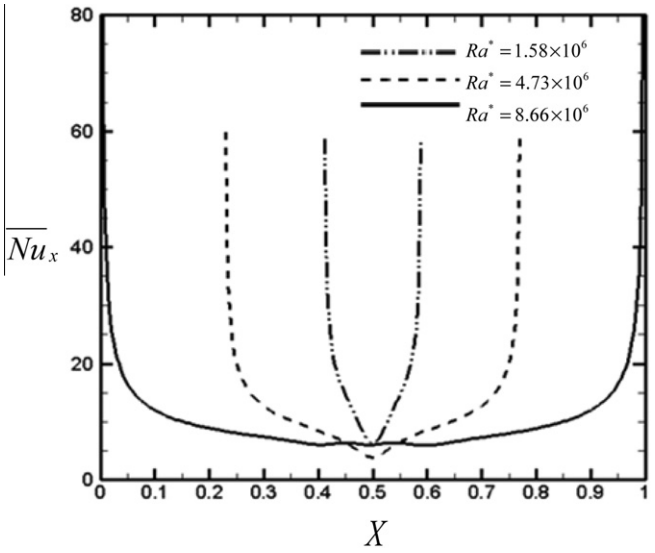

Fig. 11. Distributions of time average local Nusselt numbers under different modified Rayleigh numbers.

of circulations appear simultaneously. In Fig. 7(b) two couples of circulations are sequentially enlarged and raised by the strong strength of the buoyancy force. Meanwhile, two new circulations are also produced as fluids are sucked from the apertures. In Fig. 7(c), the appearance of phenomena of thermal and flow fields similar to those indicated in the above time steps are repeatedly observed. Afterward, in Fig. 7(d) behaviors of union of circulations happen and two residual circulations ascend continuously. Shortly, in Fig. 7(e) the unexpected appearance of the simple structures of thermal and flow fields similar to Fig. 5(c) display instantaneously. Before the time of $t^* = 1.219 \times 10^{-2}$, basically the variations of thermal and flow fields are symmetric based on the centerline and similar to those shown in Fig. 6. The buoyancy force in the situation is stronger than that of the above situation. The symmetric variations of thermal and flow fields based on the centerline have difficulty to sustain after all. As a result, shown in Fig. 6(f), the thermal and flow fields separately distributed in both half regions begin to swing unsteadily, and the circulation in the right region is somewhat suppressed by that in the left region. Oppositely, in Fig. 7(g) the circulation in the left side is suppressed by that in the right side. Behaviors of unsteady swing appear continuously and are no longer symmetrical based on the centerline. The differences between both behaviors indicated in Figs. 6 and 7 are impressive.

In Fig. 8(a), a time-averaged streamline close to the wall on the central cross section of the *XY* plane is indicated under the $Ra^* = 4.73 \times 10^6$ situation. Points of 1–7 from the inlet to outlet present corresponding locations on the streamline. Computational grids have difficulty to match the points of 1–7 exactly, then the closest computational grids corresponding to the points of 1–7 are selected. Variations of resultant velocity $V_{mag}\left(=(U^2+V^2+W^2)^{\frac{1}{2}}\right)$ with time at each point are shown in Fig. 8(b). From point 1, fluids begin to be heated, and the buoyancy force is induced simultaneously. A slight fluctuation of the variation of resultant velocity V_{mag} at this location is observed, and magnitudes of V_{mag}'s are small. Accompanied with fluids close to the central location of the heated bottom wall, fluids are continuously heated by the heat bottom wall that causes the strength of the buoyancy force to become stronger gradually. As a result, the indication of the fluctuating variation of V_{mag} is more and more remarkable until point 4. After point 4, fluids are no longer heated which means the strength of the buoyancy force is not stronger. Then the indication of the fluctuating variation of V_{mag} will decay little by little until fluids flow to the outside. In this work, the heated wall is installed horizontally and vertical to the direction of gravity. Except the central region, the flowing direction of streamline mentioned above is mainly affected by both factors of supplement of a vacant space induced by fluids discharged to the outside and a variable buoyancy force. This reason is suggested to cause the appearance of the fluctuation phenomenon mentioned earlier even in the situation of a low magnitude of V_{mag}. Also, the influence of the fluctuation phenomenon in the former region of the streamline is naturally transferred to the latter region of the streamline. Consequently, the fluctuating variations of resultant velocities display in the whole region.

In Fig. 9, the magnitude of the modified Rayleigh number is equal to 1.58×10^6. Due to the short length of the heated bottom wall, the strength of the buoyancy force is then smaller than that shown in Fig. 8. Except the initial stage, the fluctuating variation of the resultant velocity is hardly observed in the whole streamline.

In Fig. 10, the magnitude of the modified Rayleigh number is equal to 8.66×10^6. Opposite to that indicated in Fig. 9, the length of the heated bottom wall is long, which directly leads the strength of the buoyancy force to become stronger. As a result, the fluctuating variation of the resultant velocity becomes more drastic and irregular than those shown in Figs. 8 and 9.

Distributions of time-averaged local Nusselt numbers under different magnitudes of modified Rayleigh numbers are separately indicated in Fig. 11. Cool fluids are sucked from the outside, and then near the aperture region excellent heat transfer rates can be achieved. Oppositely, close to the central region, heated fluids are accumulated which causes an inferior heat transfer rate to be observed. From Fig. 6 that heated fluids still stagnantly accumulate in the central region can be observed, and in Fig. 7 heated fluids swing around the central region uninterruptedly. As a result, in the central region time-averaged local Nusselt numbers of the $Ra^* = 8.66 \times 10^6$ are slightly larger than those of the $Ra^* = 4.73 \times 10^6$.

In Fig. 12, variations of area average Nusselt numbers with t^* are shown under different magnitudes of modified Rayleigh numbers. The definition of area average Nusselt number $\overline{Nu}_A$ is expressed as follows.

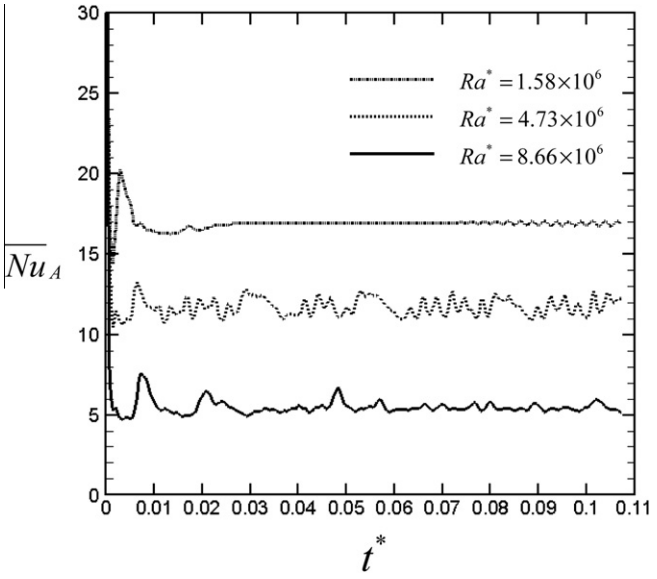

Fig. 12. Distributions of variations of area average Nusselt numbers with time under different modified Rayleigh numbers.

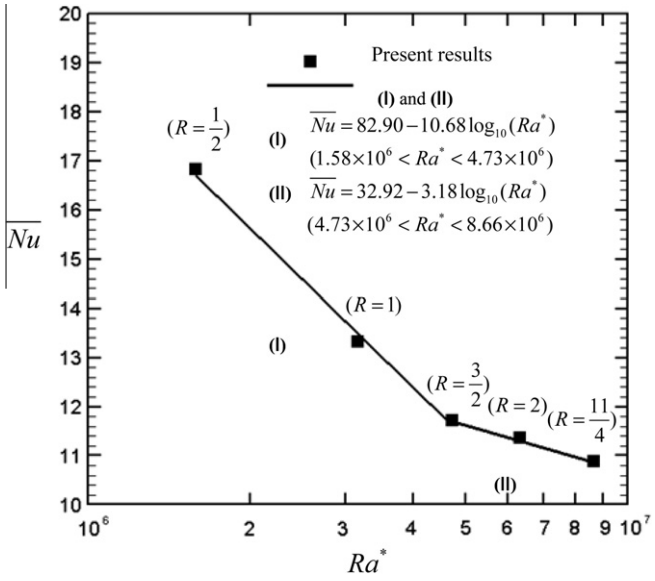

Fig. 13. Correction equations of regions of (I) and (II).

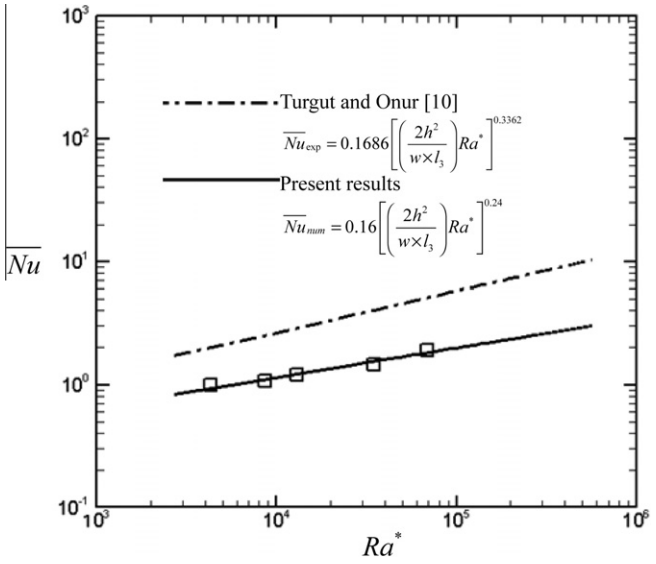

Fig. 14. Comparison of present result and results of Kitamura and Asakawa [9].

$$\overline{Nu}_A = \frac{1}{A}\int_d \int_{l_1} Nu_x dxdz \tag{30}$$

According to the results of the fluctuating variation of the resultant velocity mentioned above, in the situation of the $Ra^* = 1.58 \times 10^6$, except the initial stage, the variation of area average Nusselt numbers with t^* is nearly flat which means this situation is steady. In the situation of the $Ra^* = 4.73 \times 10^6$, the variation of area average Nusselt numbers is somewhat like periodic variation that is reasonably consistent with the fluctuating variation of the resultant velocity shown in Fig. 6. At the situation of the $Ra^* = 8.66 \times 10^6$, the indication of variation of area average Nusselt numbers is rather irregular, and periodic characteristics are difficult to be observed. These behaviors can be regarded as an unsteady situation.

Fig. 13 shows the correlation equations of the modified Rayleigh number and average Nusselt numbers derived from the results of (I) and (II) regions, respectively. The definition of an average Nusselt number $\overline{Nu}$ is expressed as follows.

$$\overline{Nu} = \frac{1}{A}\int_d \int_{l_1} \overline{Nu}_x dxdz \tag{31}$$

In the region (I), the flow and thermal fields mentioned above are under a broadly steady situation. The average Nusselt number then decreases steadily accompanied with increasement of the length of the heated surface. Beyond the length of the heated surface about $R^* = \frac{3}{2}$, according to the statements mentioned above, both flow and thermal fields begin to swing based on the center of the channel that causes the average Nusselt number to be increased. Consequently, the decreasing rate of average Nusselt numbers in the region (II) becomes small, and the variations of average Nusselt numbers in the region (II) are then no longer the same as those in region (I). Reasonably, the variation of average Nusselt numbers has a turn around $R^* = \frac{3}{2}$.

In Fig. 14, the results of this study are compared with the experimental results of Turgut and Onur [10]. The model investigated in [10] was natural convection in parallel rectangular plates that is different from the model used in this study. The model used in [10] had four apertures which allow cooling fluids to flow into and out of the model. However, in the present work, two apertures are set on two sides to allow cooling fluids to flow into and out of the model and the other two sides are periodic condition. As a result, that the ability of heat transfer of [10] caused by the cooling fluids mentioned above is approximately twice as large as that of the present work can be reasonably inferred, Both results indicated in Fig. 14 have a similar trend which indicates the rationality of the present work.

5. Conclusions

Variations of natural convection in three dimensional horizontal parallel plates with a heated bottom surface from a steady to an unsteady situation are investigated numerically. Some conclusions are drawn as follows.

(1) By way of elongating the length of the heated bottom surface, behaviors of both thermal and flow fields changing from a steady to an unsteady situation are observed.
(2) Local heat transfer rates decrease drastically accompanied between the aperture and the central region.
(3) The performance of a CUDA computational platform is excellent and useful for the challenges of three dimensional problems.

Acknowledgment

The authors gratefully acknowledge the support of the Natural Science Council, Taiwan, ROC under Contact NSC99-2221-E-009-058.

References

[1] W. Aung, L.S. Fletcher, V. Sernas, Developing laminar free convection between vertical flat plates with asymmetric heating, Int. J. Heat Mass Transfer 15 (1972) 2293–2308.
[2] P.H. Oosthuzien, A numerical study of laminar free convective flow through a vertical open partially heated plane duct, ASME HTD 32 (1984) 41–48.
[3] S. Kim, N.K. Anand, W. Aung, Effect of wall conduction on free convection between asymmetrically heated vertical plates: uniform wall heat flux, Int. J. Heat Mass Transfer 33 (1990) 1013–1023.
[4] D. Naylor, J.M. Floryan, J.D. Tarasuk, A numerical study of developing free convection between vertical parallel plates, Trans. J. Heat Mass Transfer ASME 113 (1991) 620–626.
[5] A. La Pica, G. Rodono, R. Volpes, An experimental investigation on natural convection of air in a vertical channel, Int. J. Heat Mass Transfer 36 (1993) 611–616.

[6] W.S. Fu, C.G. Li, C.P. Huang, J.C. Huang, An investigation of a high temperature difference natural convection in a finit length channel without Boussinesq assumption, Int. J. Heat Mass Transfer 52 (2009) 2571–2580.
[7] D.D. Gray, A. Giorigini, The validity of Boussinesq approximation for liquids and gases, Int. J. Heat Mass Transfer 19 (1976) 545–551.
[8] W.S. Fu, C.G. Li, C.C. Tseng, An investigation of a dual-reflection phenomenon of a natural convection in a three dimensional horizontal channel without Boussinesq assumption, Int. J. Heat Mass Transfer 53 (2010) 1575–1585.
[9] K. Kitamura, T. Asakawa, Fluid flow and heat transfer of natural convection over upward-facing, horizontal, heated plate shrouded by a parallel insulated plate, Heat Transfer Asian Res. 29 (2000) 333–346.
[10] Oğuz Turgut, Nevzat Onur, An experimental and three-dimensional numerical study of natural convection heat transfer between two horizontal parallel plates, Int. J. Heat Mass Transfer 34 (2007) 644–652.
[11] H. Yang, Z. Zhu, J. Gilleard, Numerical simulation of thermal fluid instability between two horizontal parallel plates, Int. J. Heat Mass Transfer 44 (2001) 1485–1493.
[12] O. Manca, B. Morrone, S. Nardini, Experimental analysis of thermal instability in natural convection between horizontal parallel platesuniformly heated, J. Heat Transfer 122 (2000) 50–57.
[13] O. Manca, S. Nardini, Experimental investigation on natural convection in horizontal channels with the upper wall at uniform heat flux, Int. J. Heat Mass Transfer 50 (2007) 1075–1086.
[14] NVIDIA CUDA Compute Unified Architecture 3.0 programming Guide, NVIDIA Corporation, 2010.
[15] P.L. Roe, Approximation riemann solver, parameter, vectors and difference schemes, J. Comput. Phys. 43 (1981) 357–372.
[16] J.M. Weiss, W.A. Simth, Preconditioning applied to variable and constants density flows, AIAA 33 (1995) 2050–2056.
[17] X.F. Xu, J.S. Lee, R.H. Pletcher, A compressible finite volume formulation for large eddy simulation of turbulent pipe flows at low Mach number in Cartesian coordinates, J. Comput. Phys. 203 (2005) 22–48.
[18] S. Yoon, A. Jamesont, Lower–upper symmetric-Gauss–Seidel method for the Euler and Navier–Stokes equations, AIAA 26 (1988) 1025–1026.
[19] I. Abalakin, A. Dervieux, T. Kozubskaya, A vertex centered high order MUSCL scheme applying to linearised Euler acoustics, INRIA 4459 (2002).
[20] T.J. Poinsot, S.K. Lele, Boundary conditions for Navier–Stokes, J. Comput. Phys. 101 (1992) 104–129.